

Super deformability and thermoelectricity of bulk *γ*-InSe single crystals

Bin Zhang(张斌), Hong Wu(吴宏), Kunling Peng(彭坤岭), Xingchen Shen(沈星辰), Xiangnan Gong(公祥南), Sikang Zheng(郑思康), Xu Lu(卢旭), Guoyu Wang(王国玉), and Xiaoyuan Zhou(周小元)

Citation: Chin. Phys. B, 2021, 30 (**7**): 078101. DOI: 10.1088/1674-1056/abf133
Journal homepage: http://cpb.iphy.ac.cn; http://iopscience.iop.org/cpb

What follows is a list of articles you may be interested in

Synthesis and characterizations of boron and nitrogen co-doped high pressure and high temperature large single-crystal diamonds with increased mobility

Xin-Yuan Miao(苗辛原), Hong-An Ma(马红安), Zhuang-Fei Zhang(张壮飞), Liang-Chao Chen(陈良超), Li-Juan Zhou(周丽娟), Min-Si Li(李敏斯), and Xiao-Peng Jia(贾晓鹏)

Chin. Phys. B, 2021, 30 (**6**): 068102. DOI: 10.1088/1674-1056/abf12c

Excellent thermal stability and thermoelectric properties of *Pnma*-phase SnSe in middle temperature aerobic environment

Yu Tang(唐语), Decong Li(李德聪), Zhong Chen(陈钟), Shuping Deng(邓书平), Luqi Sun(孙璐琪), Wenting Liu(刘文婷), Lanxian Shen(申兰先), Shukang Deng(邓书康)

Chin. Phys. B, 2018, 27 (**11**): 118105. DOI: 10.1088/1674-1056/27/11/118105

Modulated thermal transport for flexural and in-plane phonons in double-stub graphene nanoribbons

Chang-Ning Pan(潘长宁), Meng-Qiu Long(龙孟秋), Jun He(何军)

Chin. Phys. B, 2018, 27 (**8**): 088101. DOI: 10.1088/1674-1056/27/8/088101

Tunable thermoelectric properties in bended graphene nanoribbons

Chang-Ning Pan(潘长宁), Jun He(何军), Mao-Fa Fang(方卯发)

Chin. Phys. B, 2016, 25 (**7**): 078102. DOI: 10.1088/1674-1056/25/7/078102

Improved thermoelectric property of cation-substituted $CaMnO_3$

Pradeep Kumar, Subhash C. Kashyap, Vijay Kumar Sharma, H. C. Gupta

Chin. Phys. B, 2015, 24 (**9**): 098101. DOI: 10.1088/1674-1056/24/9/098101

Super deformability and thermoelectricity of bulk γ-InSe single crystals*

Bin Zhang(张斌)[1], Hong Wu(吴宏)[2], Kunling Peng(彭坤岭)[2], Xingchen Shen(沈星辰)[2], Xiangnan Gong(公祥南)[1], Sikang Zheng(郑思康)[2], Xu Lu(卢旭)[2], Guoyu Wang(王国玉)[4], and Xiaoyuan Zhou(周小元)[1,2,†]

[1] *Analytical and Testing Center of Chongqing University, Chongqing* 401331, *China*
[2] *Chongqing Key Laboratory of Soft Condensed Matter Physics and Smart Materials, College of Physics, Chongqing University, Chongqing* 401331, *China*
[3] *Chongqing Institute of Green and Intelligent Technology, Chinese Academy of Sciences, Chongqing* 400714, *China*
[4] *University of Chinese Academy of Sciences, Beijing* 100044, *China*

(Received 29 January 2021; revised manuscript received 16 March 2021; accepted manuscript online 24 March 2021)

Indium selenide, a III–V group semiconductor with layered structure, attracts intense attention in various photoelectric applications, due to its outstanding properties. Here, we report super deformability and thermoelectricity of γ-InSe single crystals grown by modified Bridgeman method. The crystal structure of InSe is studied systematically by transmission electron microscopy methods combined with x-ray diffraction and Raman spectroscopy. The predominate phase of γ-InSe with dense stacking faults and local multiphases is directly demonstrated at atomic scale. The bulk γ-InSe crystals demonstrate surprisingly high intrinsic super deformative ability which is highly pliable with bending strains exceeding 12.5% and 264% extension by rolling. At the meantime, InSe also possesses graphite-like features which is printable, writable, and erasable. Finally, the thermoelectric properties of γ-InSe bulk single crystals are preliminary studied and thermal conductivity can be further reduced via bending-induced defects. These findings will enrich the knowledge of structural and mechanical properties' flexibility of InSe and shed lights on the intrinsic and unique mechanical properties of InSe polytypes.

Keywords: γ-InSe single crystals, structure identification, super deformability, thermoelectric properties

PACS: 81.10.Fq, 84.60.Rb **DOI:** 10.1088/1674-1056/abf133

1. Introduction

In common sense, most inorganic semiconductors are usually brittle with poor mechanical properties. Seeking "soft" inorganic semiconductors with good mechanical behavior has drawn increasing interest, which is vital for developing flexible functional photoelectric devices. Very recently, an unusual mechanical behavior with super-plasticity/ductility on bulk-InSe single crystals was reported[1,2] which will bring new opportunities for two-dimensional (2D) field and flexible electronics.[1,2] Actually, indium selenide (InSe), a III–V group semiconductor with layered structure, has been well known in various photoelectric fields due to its promising properties for potential applications in nanoelectronics,[3] nanophotonics,[4] thermoelectrics,[5] and flexible sensors.[6] In addition to the recent report on super-plasticity of β-InSe single crystals,[1,2] the mechanical properties of InSe have been intensely studied in the last decades.[7–12] The elastic modulus of bulk γ-InSe single crystal is given as 283 GPa by nano-indentation measurements.[12] While, using the atomic force microscope (AFM), Li *et al.*[8] measured the Young's modulus to be 101.37 ± 17.93 GPa in the multilayer 2D γ-InSe (> 5 L) which is much higher than its bulk counterpart but softer than most existing 2D materials.

In ambient conditions, InSe crystals usually possess three polytype layered structures, i.e., two hexagonal phases of β-type[13–16] and ε-type[17–20] and one rhombohedral phase of γ-type,[14,16,19,20] as shown in Fig. 1(a). All these layered structures are constituted by the same primitive layered blocks. Each unit layer consists of covalently bonded Se–In–In–Se intraplanes that are connected by weak Van der Waals interactions. The stacking sequences, that is, the key features of structural differences among different phases, are demonstrated as ABAB$\cdots$ in both β and ε phases, and ABCABC$\cdots$ in γ phase. Basically, different InSe polytypes have similar constant a and b, while constant c usually corresponds to the number of primitive layers in a unit cell, i.e., $a = b = 4.05$ Å, $c = 16.93$ Å (contains 2 unit layers) for both β and ε phases[17,21] and $a = b = 4.00$ Å, $c = 25.32$ Å (3 layers) for γ phase.[22] To verify the actual structure of InSe polytypes, x-ray diffraction (XRD) alone is generally not accurate enough due to its strongly [00l] texture and very similar layered structure. In contrast, other techniques as Raman and infrared spectroscopy,[23–25] which are sensitive to the structure vibrational modes, are often combined with XRD to do the structural identification

*Project supported by the National Natural Science Foundation of China (Grant Nos. 11674040, 11604032, 51472036, 51672270, and 11904039), the Fundamental Research Funds for the Central Universities, China (Grant No. 106112016CDJZR308808), and Key Research Program of Frontier Sciences, Chinese Academy of Sciences (Grant No. QYZDB-SSW-SLH016).

†Corresponding author. E-mail: xiaoyuan2013@cqu.edu.cn

© 2021 Chinese Physical Society and IOP Publishing Ltd

of InSe. Nowadays, the advanced electron transmission microscopy (TEM), especially the spherical-aberration corrected high angle annular dark field (Cs-corrected HAADF) imaging which gives out the atomic arrangements directly, has been widely applied for atomic structure analysis and a few reports on InSe were found.[18,26] Despite the common β-, γ-, and ε-InSe polytypes, structural defects as plenty of stacking faults, twins, and local multiphases were also claimed to be present in InSe matrix[27,28] and three new layered polytypes as *Pm1*, $P6_3mc$, and *Rm* phases were theoretically predicted.[29] Moreover, it is worth noting that several nonlayered metastable phases also exist, such as zinc blende cubic structure in InSe nanomaterials[30,31] and monoclinic or NaCl-like cubic structure under high pressure and high temperature.[32] Generally, the knowledge of atomic structure is fundamental to the understanding of the physical properties, however different structural variations and abundant defects in InSe result in the difficulty in its structure determination. Therefore, accurate and comprehensive methods as well as special attention are highly desired in the structure determination of InSe-based materials.

Two-dimensional materials, owing to the intrinsically layered structure that is favorable for achieving a low lattice thermal conductivity, have been widely regarded as good candidates for thermoelectric materials. As typical 2D structures, indium selenides materials have been received growing attention in thermoelectrics owing to their intrinsic structural characteristics. For instance, the zT value of ~ 1.48 at 705 K in $In_4Se_{3-\delta}$ was obtained, which is resulted from the low lattice thermal conductivity and the high Seebeck coefficient,[33] and the zT of ~ 1.23 at 916 K was reported in Zn-doped In_2Se_3.[34] Meanwhile, a peak zT value of ~ 0.23 in Sn doped InSe polycrystalline material,[35] and ~ 0.14 in Si-doped InSe[36] were reported. In recent years, remarkable achievements have been achieved in single crystalline thermoelectric materials. Promising thermoelectric properties were reported in various 2D materials' single crystals, such as Na-doped SnSe,[37] SnS,[38] and $SnS_{0.91}Se_{0.09}$,[39] single crystals, and Br-doped SnSe single crystal.[40] However, intrinsic thermoelectric properties of InSe single crystals and the enhancement are still largely unknown.

In this work, γ-InSe bulk single-crystal ingots were grown via a modified Bridgeman method. Through comprehensive analysis of XRD, TEM, and Raman spectroscopy, the structure of InSe bulk crystals was systematically studied. The as-grown InSe ingot predominantly took the γ phase with plenty of stacking faults and coexistence of local multiphases. The γ-InSe bulk crystals also exhibited superior mechanical behaviors with super-plasticity as discovered in its β-type.[1] Finally, the thermoelectric performance of InSe bulk crystal was initially studied which showed an extraordinarily high thermal conductivity and it could be significantly reduced via bending/deformations.

2. Experiments and methods

2.1. Growth of InSe bulk crystal

Stoichiometric amounts of high purity elements In filament (99.999%) and Se powder (99.99%) of InSe were weighed and then loaded into cone-shaped silica tubes ($\phi =$ 16 mm) under an argon atmosphere. The tubes were sealed under $\sim 5 \times 10^{-4}$ Pa and placed in another quartz tubes (larger diameter, $\phi = 13$ mm). The silica tubes were slowly heated up to 1273 K over 20 h, soaked at this temperature for 10 h, and subsequently cooled to 973 K as they were moving at a rate of 1.5 mm·h^{-1}. Finally, InSe bulk crystal ingot with dimensions of 14 mm (diameter) $\times$40 mm (length) was obtained (Fig. S1(a)).

2.2. Characterization

The powder was scraped from the as-grown InSe ingot and slightly grounded for XRD measurement using a PANalytical X'Pert diffractometer with Cu $K\alpha$ radiation at 40 kV and 40 mA. Raman spectroscopy was carried out with HORIBA JobinYvon HR Evolution, 1800 groove/mm holographic grating, and a thermoelectric cooled synapse charge coupled device (CCD) for high spectra resolution, and a solid-state Nd: YAG laser with the wavelength of 532 nm as the excitation source. Several InSe bulk crystal wafers/foils (Fig. S1(b)) with a few millimeters in length/width and submillimeter in thickness were exfoliated from the InSe ingot for scanning electron microscopy (SEM) and mechanical analysis. The SEM image and energy dispersive x-ray spectroscopy (EDS) mapping were obtained via a Thermofisher Scientific Quattro S microscope. The InSe nanoflakes were prepared by the classical exfoliation method with a tape (SPV-224S), while the cross-sectional samples were prepared by focused ion beam (FIB, Zesis Auriga Compact) for TEM studies. The selected area electron diffraction (SAED), high resolution TEM (HRTEM), HAADF images, and EDS mapping were obtained on a Thermoscientific Talos F200S microscope at 200 kV or a probe-corrected Titan Themis microscope at 300 kV. HAADF simulations were performed by using KineHAADF program.[41] Finally, the carrier concentration and the thermoelectric performance were measured by Physical Property Measurement System (PPMS) DynaCool 9.

3. Results and discussion

3.1. Structure analysis

Figure 1(b) shows the XRD pattern of InSe powder. All the main peaks can be indexed to the $(00l)$ reflections, indi-

cating a strong [00l] texture, due to its inherent layered structure. Because of the similar layered structures among different phases, the precise phase composition cannot be convinced ($00l$) peaks in XRD. Some weak peaks in the XRD patterns are visible as well, but not precise enough for structure determination among InSe polytypes. This is because dense diffraction peaks appear in the simulated XRD patterns of all the InSe structures (the lower panel of Fig. 1(b)), meaning some weak peaks may also ascribe to different structures. Thus, the actual structure of the InSe cannot be precisely clarified based on the present XRD pattern (Fig. 1(b)), detailed structural analysis is necessary. The morphology of the cleavage surface and cross-sectional fracture (perpendicular to the cleavage surface) of the present InSe bulk was obtained by SEM and shown in Figs. 2(a) and 2(b). The dense parallel striations are presented in the fracture section. The SEM-EDS mappings were taken on the cleaved surface, as seen in Figs. 2(c) and 2(d). In addition, STEM-EDS mappings on the InSe nanoflakes were obtained as depicted in Figs. 2(e)–2(g). Both of them demonstrate the uniform element distribution of InSe at various scales. The chemical composition is identified as atomic ratio of In:Se = 48.5 : 51.5 (by SEM-EDS) and 49.7:50.3 (by STEM-EDS), which is close to the nominal composition of InSe.

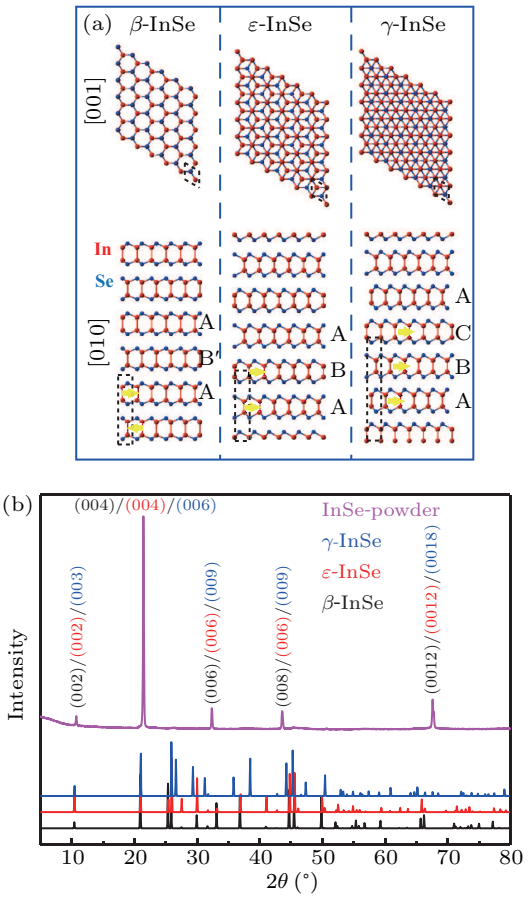


Fig. 1. (a) Structure models of InSe polytype layered structures. (b) XRD patterns of InSe powder accompanied by simulated XRD spectra.

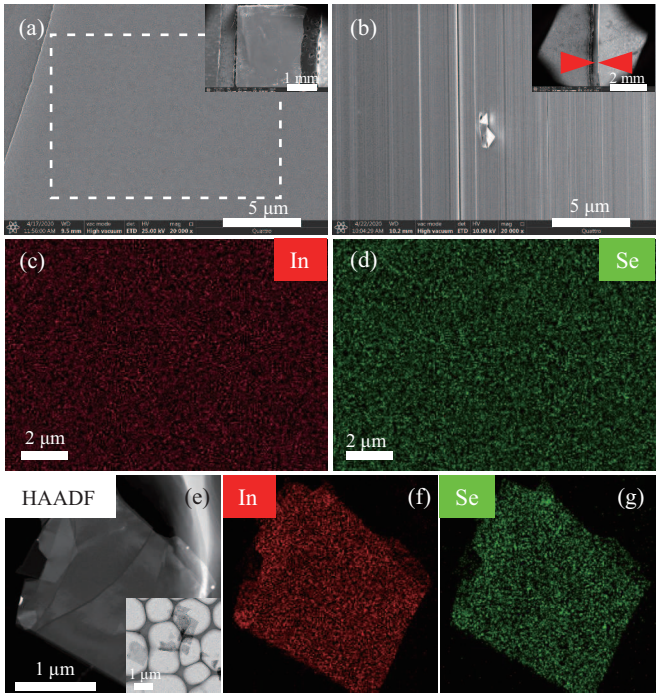


Fig. 2. (a), (b) SEM images of in-plane (a) and cross section (b) surfaces of bulk InSe, respectively. (c), (d) SEM-EDS mappings corresponding to the dotted region in (a). (e)–(g) STEM-EDS mappings of InSe nanoflakes.

To reveal the actual structure of InSe at atomic scale, systematical TEM studies were performed. Firstly, the SAED pattern, HRTEM, and HAADF images of the exfoliated InSe nanosheet were obtained along the [001] direction, as shown in Figs. 3(a)–3(c). When compared with the simulated SAED patterns (Fig. S2(b)), the experimental pattern (Fig. 3(a)) seems to belong to a hexagonal phase (β- or ε-InSe) or at least a mixed structure of hexagonal and rhombohedral phases (γ-InSe). Recently, a similar [001] SAED pattern was reported by Sun *et al.*,[17] and it was claimed to be a ε-InSe single crystal. However, InSe bulk crystal in the present work is predominately γ-type instead of ε-type as confirmed by the following comprehensive analysis. Therefore, it seems that the [001] SAED pattern alone is generally not accurate enough for InSe structure determination. Regarding to the HRTEM image (Fig. 3(b)), the regular lattices/dots can be roughly divided into three groups based on the image contrast, that is, one centered dimmest dot, three dimmer and three brighter dots (indicated by the circles) as surroundings. Thus, the HRTEM image suggests a 3-fold symmetry, which is suggested to be an indication of rhombohedral structure, i.e., γ-InSe. Moreover, the [001] HAADF image (Fig. 3(c)) presents a regular hexagonal lattice with uniform contrast/intensity, which is well consistent with the simulated HAADF image of γ-InSe but significantly different from that of β- or ε-InSe (see Fig. S3), further suggesting the γ-InSe of the present sample. Subsequently, the sample was continuously tilted to another zone axis, and the corresponding SAED and HRTEM images were obtained (Figs. 3(d) and 3(e)). Correspondingly, the same tilting operations (with the same tilting directions and angles)

were carried on these polytype structure models. The corresponding atomic projections and diffraction patterns were presented in Figs. S2(a) and S2(b). Expectedly, the SAED pattern (Fig. 3(d)) can be well indexed to the $[\bar{4}\bar{2}1]$ zone axis of γ-InSe, but different from the patterns of β- and ε-InSe as revealed in Fig. S2(a). Similar analysis (serially tilted SAED patterns and HRTEM images) and results were obtained on several InSe nanoflakes. Therefore, on the basis of TEM analysis, it is concluded that the predominate structure of the present InSe is γ phase, but the coexistence of β and ε phases still cannot be completely excluded. According to the literature, it seems that InSe single crystals grown by Bridgeman method prefer to form γ phase,[21,42–47] and other polytypes of β-InSe[1] and ε-InSe[17,18] single crystals were occasionally reported.

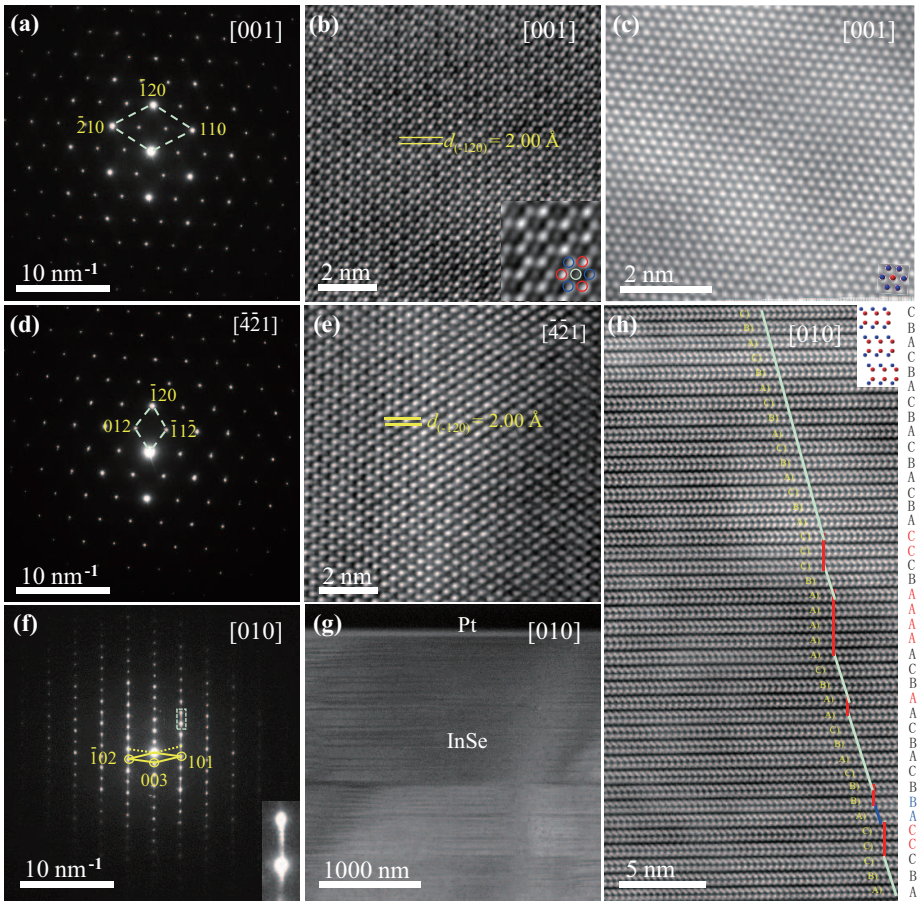


Fig. 3. TEM characterization of InSe crystals. (a)–(c) SAED pattern, the filtered HRTEM and HAADF images of the exfoliated nanosheets, along the [001] direction, respectively. (d), (e) SAED pattern and HRTEM image under the [1] zone axis through sample tilting, respectively. (f)–(h) SAED pattern, BF-TEM image, and HAADF image of the cross-sectional sample, respectively. Atomic models of γ-InSe are attached on the HAADF images.

As a matter of fact, cross-sectional samples (e.g., along the [010] direction, the same for the [100] direction) are more straightforward for structural determination through the direct observation of stacking sequence. Most of the pervious SAED patterns and HRTEM images were taken along the [001] zone axis,[1,17,21,23,42–45,48,49] which is a top view of the unit layer but instead of a side view of the cross section. Recently, based on the [100] HAADF images, Hao *et al.*,[18] clearly showed atomically resolved picture of ABAB$\cdots$ stacking sequence of ε-InSe phase on bulk single crystal, while Wu *et al.*[26] revealed ABCABC$\cdots$ arrangement of γ-InSe based on a InSe/hBN/graphite heterostructure of thin films. In the present work, cross-sectional samples were prepared by FIB and further analyzed by HAADF imaging for stacking sequence investigation. The SAED pattern (Fig. 3(f)) can be well indexed to the [010] zone axis of γ-InSe but completely different from that of β- and ε-InSe, as compared to the simulated patterns in Fig. S2(c). The appearance of surrounding satellite spots in the SAED pattern further suggests the existence of stacking faults. A similar SAED pattern with satellite spots was also noted in the ε-InSe single crystal[18] with stacking faults. Rigoult *et al.* claimed that the amount of stacking faults in the γ-InSe single crystals could be as large as $\sim 6\%$ based on the XRD refinement.[27] Here, the appearance of stacking faults is further confirmed by a bright field (BF) TEM image with high density of "straight line" features, as seen in Fig. 3(g). As expected, the atomic-scale HAADF image (Fig. 3(h)) reveals that the matrix is indeed γ-InSe with ABCABC$\cdots$ stacking sequence as guided by the white lines. But local ε phase with ABAB$\cdots$ (guided by the bule lines) and abnormal AA$\cdots$ (by the red lines, even might be a new phase) stacking sequences also coexist. Moreover, local β-InSe, twins, and other defective structures were also observed (Fig. S4). Generally, the present bulk γ-InSe with coexistence of dense stacking faults

and multiphases/impurifies was vividly identified by the comprehensive TEM analysis. When revisiting the [001] SAED pattern, we found that the experimental pattern (Fig. 3(a)) exhibits several extinction diffraction spots as compared to the theoretical one (Fig. S2(b)) of γ-InSe. These extinction diffraction spots could be ascribed to the above structural modifications, i.e., stacking faults and local multiphases. Interestingly and notably, when the sample tilted from the [010] to [120] zones, a feature of perfect "single crystal" was presented (Fig. S5), and all the features of stacking faults and local multiphases "disappeared". This is because the polytype InSe possesses the same atomic arrangement projections along the [120] zone as shown in Fig. S2(d).

Raman spectroscopy was further performed on the exfoliated InSe flakes as displayed in Fig. S6. Generally, the Raman peaks in Fig. S6(b) at 40 cm^{-1}, 115 cm^{-1} 177 cm^{-1}, and 226 cm^{-1} are common in both β-, γ-, and ε-InSe phases.[17,18] However, the Raman peak around 199 cm^{-1} is thought to originate from the non-centrosymmetric structures as ε or γ phase.[17–20] Consequently, the $\sim$ 199 cm^{-1} peak here could be resulted from γ-InSe. Additionally, Raman spectrum in Fig. S6(b) shows significant thickness-dependence. Specifically, as the thickness decreases, the $\sim$ 199 cm^{-1} peak gradually separates into two shoulder peaks. It is found that such separated peaks were also observed in the ε-InSe.[21] Therefore, this peak splitting might be ascribed to the increased proportion of stacking faults or local impurities (as confirmed above) in the nano-thick γ-InSe flakes. Finally, based on the above analysis, we conclude that the predominate γ-phase with plenty of stacking faults and coexistence of local multiphases is present in bulk InSe single crystals grown by the modified Bridgeman method.

3.2. Mechanical property analysis

To investigate the mechanical behavior of the present γ-InSe single crystals, several bulk slices with sub-mm thickness were prepared. The morphology evolution of InSe slices during bending deformation was studied by SEM, as shown in Fig. 4(a). In the initial state of InSe slice/foil (marked as initial 0° state), typical "parallel striations" features parallel to the cleavage surface were found (Figs. 4(a4) and 4(a5)).

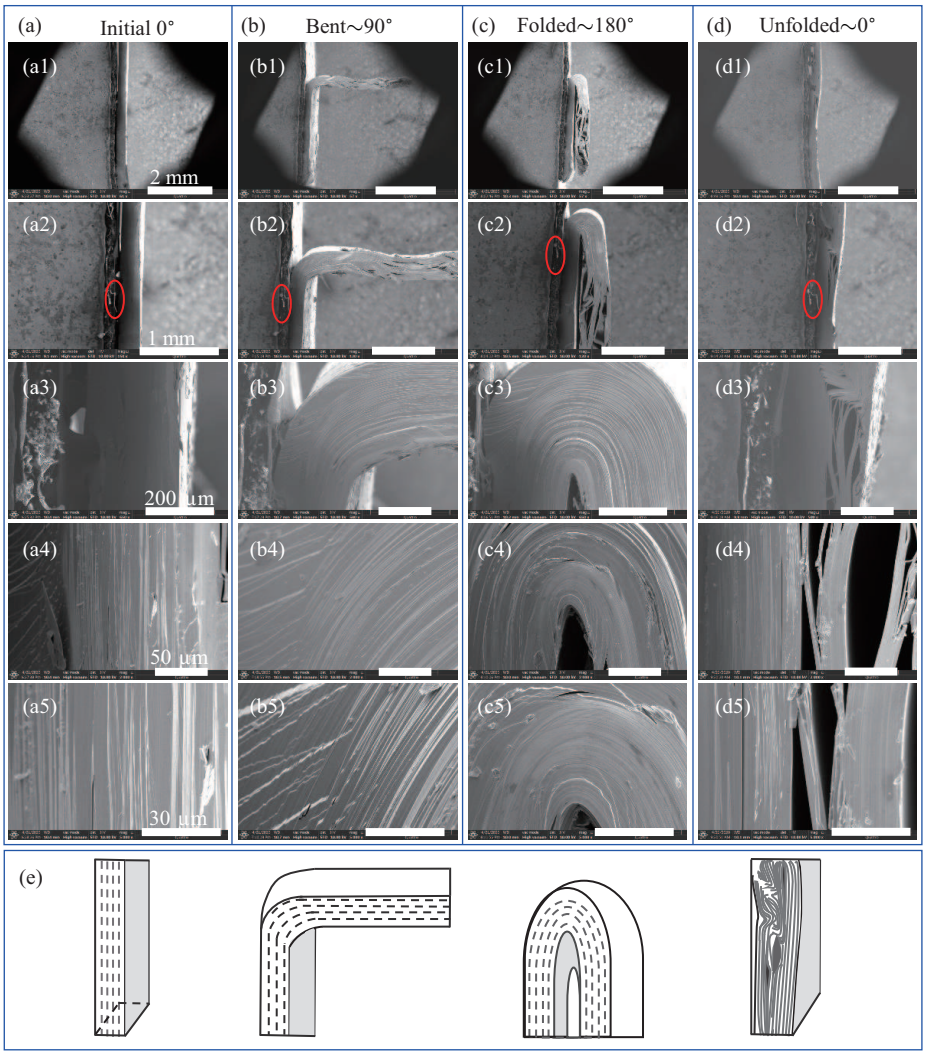


Fig. 4. The morphology evolution of γ-InSe slices/foils during bending deformation observed by SEM: (a) the original state ($\sim 0°$), (b) bending of $\sim 90°$, (c) bending of $\sim 180°$ (folded), (d) return to $\sim 0°$ (unfolded). The red circles are markers for indicating the root of the bending InSe in (a2)–(d2). (e) The schematic for the bending deformation process.

Subsequently, InSe bulk slice was gently bent to ∼ 90° (Fig. 4(b)) and ∼ 180° (Fig. 4(c)). Interestingly, no embrittlement or cracking was observed at the bending root, and the initial "parallel striations" were gradually bent simultaneously. Finally, after a recovery treatment the sample was nearly returned to the ∼ 0° state, with some cracks and wrinkles being left inside the InSe slice (Fig. 4(d)). Schematic illustrations of the deformation process are shown in Fig. 4(e). Additionally, several similar cases related to the bending performance of InSe slices were shown in Figs. S7 and S8, which further confirm the good plasticity of the γ-InSe. Detailed morphology observations of normal and bending of InSe were depicted in Fig. S8.

Desides the bending deformation, γ-InSe bulk was further deformed by rolling. As shown in Figs. 5(a)–5(d), original InSe bulk was enlarged gradually during the continuously rolling process under the compressive and shear stress. Areas of this InSe bulk at different stages (Fig. 5) were roughly estimated based on the projection of the sample by using the particle analysis tool in Digital Micrograph software. The projected area of the sample increased from the initial 62.3 mm^2 (Fig. 5(a)) to the final 164.6 mm^2 (Fig. 5(d)), with an expansion of about ∼ 264%. Both the above bending and rolling experiments and results show that γ-InSe single crystal has good plasticity and ductility, which are similar to the recently reported β-type.[1,2] In addition to the super deformability, it is interesting to note that InSe ingot can be written smoothly like graphite/pencil and also be erased, as shown in Figs. 5(e) and 5(f). This indicates that InSe is similar to graphite which is also a printable, writable, and erasable material.

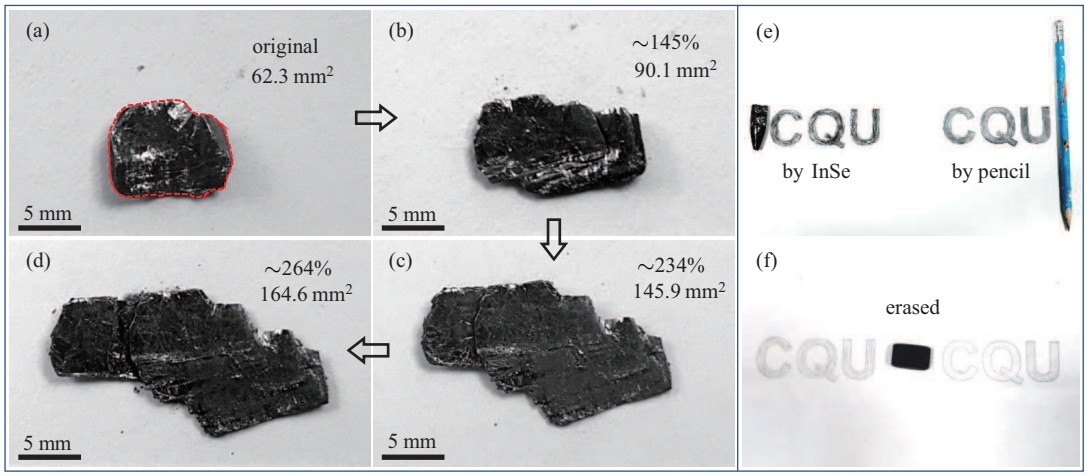


Fig. 5. (a)–(d) The ductility of γ-InSe under rolling. The red dotted line (in (a)) indicates the projection area for evaluation. (e), (f) The writing experiment of InSe ingot (e) compared with HB pencil (f), respectively.

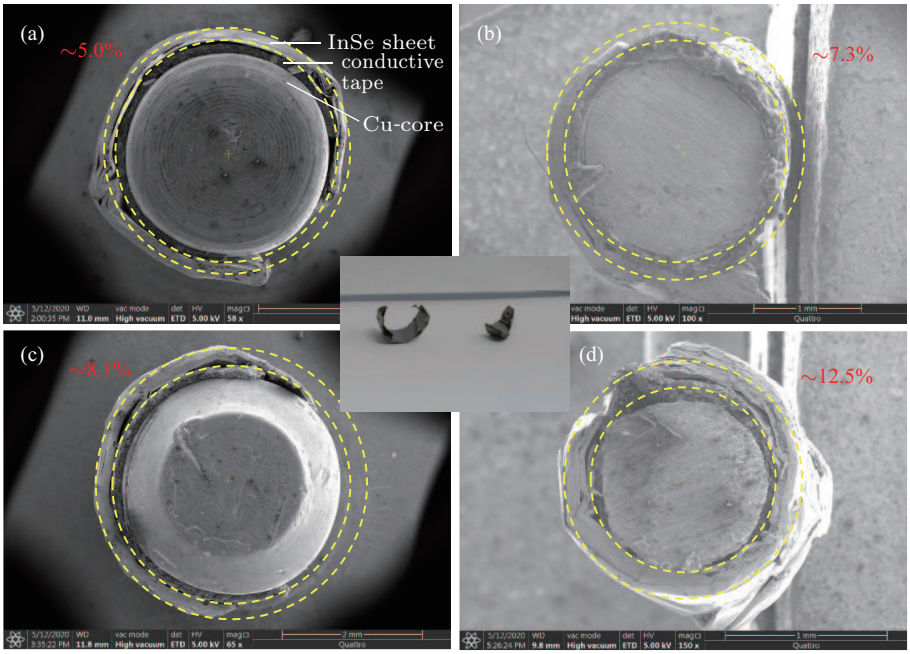


Fig. 6. Wrapping the InSe slices on the surface of the copper wires.

For comparison, similar bending experiments were conducted on bulk graphite, i.e., the commercial highly oriented pyrolytic graphite (HOPG) with comparable thickness of a few hundred micrometers. Unlike the highly plasticity of γ-InSe, HOPG bulk is brittle as breaking or fracture occurred when under the similar bending performance (even much less than 90°), as seen in Fig. S9. In addition, γ-InSe and graphite slices were crimped on the surface of copper wires. As shown in Fig. 6, the InSe slices can uniformly be wrapped on the surface of the copper wires. Beside the internal cracks or wrinkles, InSe slices were gradually bent along the surface of the copper wire without obvious broken. At the same time, the maximum tensile strain of InSe slices on the outer surface was roughly estimated according the bending beam model. Meanwhile, the strain of the γ-InSe slices under different conditions was analyzed, and bending strain over 12.5% was achieved, as shown in Fig. 6(d). Contrarily, graphite flakes could not form a uniform coverage on the copper wire (Fig. S9) with the most area of graphite not being bent, while some brittle fracture occurred. These above findings indicate that bulk γ-InSe has superior mechanical properties than bulk HOPG. Such good mechanical properties of γ-InSe single crystal are believed to be of great value for its practice applications especially in flexible functional devices.

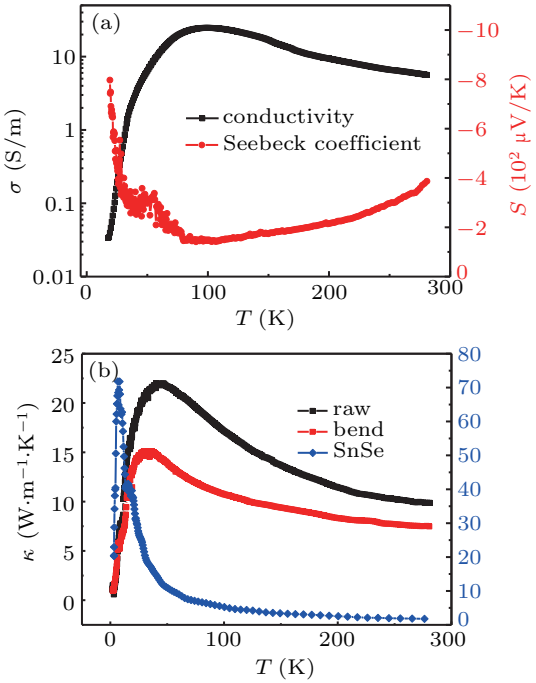


Fig. 7. The electrical and thermal transport measurement of InSe. (a) Electrical conductivity and Seebeck coefficient of InSe, (b) thermal conductivity of InSe before and after bending twice.

In the following, the TE performance of pristine γ-InSe crystals was initially studied. Figure 7(a) demonstrates the temperature-dependent Seebeck coefficient (S) and the electrical conductivity (σ) for InSe single crystal. The negative Seebeck coefficient in the whole temperature (50–280 K) region is noted, indicating the n-type semiconductors behavior. The S decreases from -796 $\mu V{\cdot}K^{-1}$ at 17 K to a minimum of -141 $\mu V{\cdot}K^{-1}$ at 100 K, increasing to -386 $\mu V{\cdot}K^{-1}$ before 280 K. As to the electricity, σ increases from 0.337 $S{\cdot}m^{-1}$ at 17 K to 24 $S{\cdot}m^{-1}$ at 80 K, and then decreases to 5.614 $S{\cdot}m^{-1}$ at 280 K. The value of σ is comparatively small due to the low carrier concentration (Fig. S10), which indicates the high quality of the as-grown InSe single crystals. Currently, a very low thermoelectric performance of InSe single crystal with zT of ~ 0.00027@280 K is obtained, mainly due to its poor electrical properties. The optimization of the electrical properties through alloying or doping to improve the thermoelectric properties of InSe-based single crystals needs further attempts. Figure 7(b) depicts the thermal conductivity as a function of temperature for InSe single crystal. Considering the low electrical conductivity, the total thermal conductivity is determined by the lattice part. Obviously, the thermal conductivity of InSe crystal sharply increases with the temperature arising from the enhanced specific heat capacity at low temperature (below 40 K), and then decreases following the T^{-1} law at higher temperatures owing to the strengthened phonons scattering, which is in good agreement with the behavior of the thermal conductivity in crystalline materials. In contrast, thermal conductivity of SnSe is much lower in the range 50–280 K as shown in Fig. 7(b), which may arise from the strong lattice anharmonicity in SnSe. As such, there is a large space to reduce the thermal conductivity for InSe system. One efficient way is to bind the sample to produce wrinkles by enhancing the phonons scattering as shown in Fig. 7(b).

4. Conclusion

In summary, bulk γ-InSe single crystals are grown by modified Bridgeman method. The predominate structure of γ-InSe with dense stacking faults and coexistence of local polytypes is identified by systematic TEM studies particularly on atomic scale analysis. The super deformable mechanical behaviors of the bulk γ-InSe crystals are discovered in γ-InSe. The thermoelectric performance of pristine bulk γ-InSe crystals is initially studied and the thermal conductivity is significantly reduced by applying plastic deformation. InSe-based materials present potentials in the application of flexible electronic devices. In addition to the super deformability, γ-InSe single crystals can also be written smoothly like graphite/pencil. These findings enrich the knowledge and clarify the underlying mechanisms of structural and mechanical property flexibility of InSe polytypes and shed light on developing mechanical plasticity and flexibility of van der Waals layered materials.

References

[1] Wei T R, Jin M, Wang Y C, Chen H Y, Gao Z Q, Zhao K P, Qiu P F, Shan Z W, Jiang J, Li R B, Chen L D, He J and Shi X 2020 *Science* **369**

542
[2] Han X D 2020 *Science* **369** 509
[3] Feng W, Zheng W, Chen X S, Liu G B and Hu P A 2015 *ACS Appl. Mater. Interfaces* **7** 26691
[4] Shubina T V, Desrat W, Moret M, Tiberj A, Briot O, Davydov V Y, Platonov A V, Semina M A and Gil B 2019 *Nat. Commun.* **10** 3479
[5] Hung N T, Nugraha A R T and Saito R 2017 *Appl. Phys. Lett.* **111** 092107
[6] Chen L, Yu Z G, Liang D, Li S F, Tan W C, Zhang Y W and Ang K W 2020 *Nano Energy* **76** 105020
[7] Panella V, Carlotti G, Socino G, Giovannini L, Eddrief M, Amimer K and Sebenne C 1997 *J. Phys.:Condens. Matter* **9** 5575
[8] Li Y H, Yu C B, Gan Y Y, Kong Y Y, Jiang P, Zou D Feng, Li P H, Yu X F, Wu R, Zhao H J, Gao C F and Li J Y 2019 *Nanotechnology* **30** 335703
[9] Sun C, Xiang H, Xu B, Xia Y D, Yin J and Liu Z G 2016 *Appl. Phys. Express* **9** 035203
[10] Li W B and Li J 2015 *Nano Res.* **8** 3796
[11] Demirci S, Avazli N, Durgun E and Cahangirov S 2017 *Phys. Rev. B* **95** 115409
[12] Mosca D H, Mattoso N, Lepienski C M, Veiga W, Mazzaro I, Etgens V H and Eddrief M 2002 *J. Appl. Phys.* **91** 140
[13] Popovic S, Tonejc A, Grzeta-Plenkovic B, Celustka B and Trojko R 1979 *J. Appl. Cryst.* **12** 416
[14] Han G, Chen Z G, Drennan J and Zou J 2014 *Small* **10** 2747
[15] Čelustka B and Popovi S 1974 *J. Phys. Chem. Solids* **35** 287
[16] Inoue S, Yoshida T and Morita T 1982 *Jpn. J. Appl. Phys.* **21** 242
[17] Sun M J, Wang W, Zhao Q H, Gan X T, Sun Y H, Jie W Q and Wang T 2020 *Cryst. Eng. Comm.* **22** 7864
[18] Hao Q Y, Yi H, Su H M, Wei B, Wang Z, Lao Z Z, Chai Y, Wang Z C, Jin C H, Dai J F and Zhang W J 2019 *Nano Lett.* **19** 2634
[19] Chen Z S, Biscaras J and Shukla A 2015 *Nanoscale* **7** 5981
[20] Grimaldi I, Gerace T, Pipta M M, Perrotta I D, Ciuchi F, Berger H, Papagno M, Castriota M and Pacilé D 2020 *Solid State Commun.* **311** 113855
[21] Yang Z B, Jie W J, Mak C H, Lin S H, Lin H H, Yang X F, Yan F, Lau S P and Hao J H 2017 *ACS Nano* **11** 4225
[22] Lokforman P A, Carré D, Etienne J and Bachet B 1975 *Acta Cryst. B* **31** 1252
[23] Wang J J, Cao F F, Jiang L, Guo Y G, Hu W P and Wan L J 2009 *J. Am. Chem. Soc.* **131** 15602
[24] Ikari T, Shigetomi S and Hashimoto K 1982 *Phys. Stat. Sol. b* **111** 477
[25] Carlone C and Jandl S 1979 *Solid State Commun.* **29** 31
[26] Wu L M, Shi J N, Zhou Z, Yan J H, Wang A W, Bian C, Ma J J, Ma R S, Liu H T, Chen J C, Yuan Huang, Zhou W, Bao L H, Ouyang M, Pantelides S T and Gao H J 2020 *Nano Res.* **13** 1127
[27] Rigoult J, Rimsky A and Kuhn A 1980 *Acta Cryst. B* **36** 916
[28] Blasi C D, Micocci G, Mongelli S and Tepore A 1982 *J. Cryst. Grow.* **57** 482
[29] Sun Y H, Li Y W, Li T S, Biswas K, Patanè A and Zhang L J 2020 *Adv. Funct. Mater.* **30** 2001920
[30] Park K H, Jang K, Kim S, Kim H J and Son S U 2006 *J. Am. Chem. Soc.* **128** 14780
[31] Ning J J, Xiao G J, Xiao N R, Wang L, Liu B B and Zou B 2011 *J. Crys. Grow.* **336** 1
[32] Errandonea D, Martínez-García D, Segura A, Chevy A, Tobias G, Canadell E and Ordejon P 2006 *Phys. Rev. B* **73** 235202
[33] Rhyee J S, Lee K H, Lee S M, Cho E, Kim S I, Lee E, Kwon Y S, Shim J H and Kotliar G 2009 *Nature* **459** 965
[34] Cui J, Wang L, Du Z, Ying P and Deng Y 2015 *J. Mater. Chem. C* **3** 9069
[35] Hou X, Chen S, Du Z, Liu X and Cui J 2015 *RSC Adv.* **5** 102856
[36] Yim J H, Park H H, Jang H W, Yoo M J, Paik D S, Baek S H and Kim J S 2012 *J. Electron. Mater.* **41** 1354
[37] Zhao L D, Lo S H, Zhang Y S, Sun H, Tan G J, Uher C, Wolverton C, Dravid V P and Kanatzidis M G 2014 *Nature* **508** 373
[38] Wu H, Lu X, Wang G Y, Peng K L, Chi H, Zhang B, Chen Y J, Li C J, Yan Y C, Guo L J, Uher C, Zhou X Y and Han X D 2018 *Adv. Energy Mater.* **8** 1800087
[39] Peng K L, Zhang B, Wu H, Cao X L, Li A, Yang D F, Lu X, Wang G Y, Han X D, Uher C and Zhou X Y 2018 *Mater. Today* **21** 501
[40] Chang C, Wu M H, He D S, Pei Y L, Wu C F, Wu X F, Yu H L, Zhu F Y, Wang K D, Chen Y, Huang L, Li J F, He J Q and Zhao L D 2018 *Science* **360** 778
[41] He D S, Li Z Y and Yuan J 2015 *Micron* **74** 47
[42] Blasi C D, Micocci G, Mongelli S, Tepore A and Zuanni F 1983 *Mater. Chem. Phys.* **9** 55
[43] Chevy A, Kuhn A and Martin M S 1977 *J. Crys. Grow.* **38** 118
[44] Wu M, Xie Q Y, Wu Y Z, Zheng J J, Wang W, He L, Wu W S and Lv B 2019 *AIP Adv.* **9** 025013
[45] Mosca D H, Mattoso N, Lepienski C M, Veiga W, Mazzaro I, Etgens V H and Eddrief M 2002 *J. Appl. Phys.* **91** 140
[46] Isik M and Gasanly N M 2020 *Mat. Sci. Semicon. Proc.* **107** 104862
[47] Julien C, Hatzikraniotis E, Chevy A and Kambas K 1985 *Mat. Res. Bull.* **20** 287
[48] Hu Y X, Feng W, Dai M J, Yang H H, Chen X S, Liu G B, Zhang S C and Hu P A 2018 *Semicond. Sci. Technol.* **33** 125002
[49] Li H, Han X, Pan D, Yan X, Wang H W, Wu C M, Cheng G H, Zhang H C, Yang S, Li B K, He H T and Wang J N 2018 *Cryst. Growth Des.* **18** 2899